IIETA International Information and Engineering Technology Association
Advancing the World of Information and Engineering

Annales de Chimie - Science des Matériaux
Vol. 49, No. 6, December, 2025, pp. 653-662
Journal homepage: http://iieta.org/journals/acsm

Photonic Control of Nanoparticle Morphology via Continuous-Wave and Femtosecond Laser Irradiation: Mechanisms, Tunability, and Emerging Applications

Shanmuga Sundari Mariyappan*, K. Kanaka Vardhini, Goguri Rashmitha

Computer Science and Engineering, BVRIT HYDERABAD College of Engineering for Women, Hyderabad 500090, India

Corresponding Author Email: sundari.m@bvrithyderabad.edu.in

https://doi.org/10.18280/acsm.490607

Received: 20 August 2025
Revised: 18 October 2025
Accepted: 25 October 2025
Available online: 31 December 2025

Keywords:
green synthesis, silver nanoparticles, femtosecond laser irradiation, continuous-wave laser processing, nanoparticle morphology and crystallinity, biomedical and environmental applications

ABSTRACT

Green synthesis combined with laser-assisted modification offers a sustainable route for tailoring the properties of silver nanoparticles (AgNPs). In this study, lemon juice extract was employed as a natural reducing and stabilizing agent to produce AgNPs, which were subsequently exposed to continuous-wave (CW) and femtosecond (fs) laser irradiation. UV–Visible Spectroscopy (UV–Vis) analysis showed a blue shift of the localized surface plasmon resonance (LSPR) peak from 435 nm (control) to 426 nm (CW) and 415 nm (fs), with spectral narrowing that reflected improved size uniformity. Transmission Electron Microscopy (TEM) measurements confirmed a reduction in mean particle size from 31.5 ± 7.8 nm (control) to 22.5 ± 4.5 nm (CW) and 16.8 ± 3.2 nm (fs), with fs irradiation also producing anisotropic features. X-Ray Diffraction (XRD) revealed retention of the face-centered cubic (FCC) structure, while crystallite size decreased from 27.8 nm (control) to 21.2 nm (CW) and 17.5 nm (fs). Fourier Transform Infrared Spectroscopy (FTIR) spectra indicated partial removal of phytochemical capping after fs exposure, and Dynamic Light Scattering (DLS) results demonstrated reduced hydrodynamic size and polydispersity index (0.276 → 0.126). Collectively, the findings highlight fs laser treatment as a powerful tool for achieving smaller, monodisperse, and structurally refined AgNPs, broadening their applicability in biomedical, catalytic, and environmental domains.

1. INTRODUCTION

Nanoparticles [1] are an indispensable class of materials whose exceptional properties arise from their nanometer-scale dimensions and high surface-to-volume ratios. At this scale, quantum confinement effects, surface plasmon resonance, and altered defect structures endow them with optical, electrical, catalytic, and biological behaviors unattainable in their bulk counterparts. Such attributes have accelerated their use in photonics, catalysis, environmental remediation, sensing, and targeted biomedical treatments. Yet, a persistent challenge in nanotechnology lies in achieving precise control over particle morphology—specifically size, shape, crystallinity, and surface chemistry—since these factors directly influence performance in end applications.

Nanoparticle performance is highly sensitive to their physical and chemical attributes. For example, smaller silver nanoparticles (AgNPs) (< 20 nm) exhibit stronger antimicrobial activity due to higher surface-to-volume ratios, while anisotropic structures such as nanorods and triangular plates generate intensified electromagnetic "hotspots" that significantly enhance SERS detection sensitivity. Surface chemistry also governs colloidal stability and biological interactions; phytochemical-capped AgNPs show enhanced biocompatibility, whereas citrate- or polymer-capped particles demonstrate different catalytic and optical responses. Likewise, crystallinity and defect density directly influence plasmonic strength, heat conversion efficiency, and catalytic reaction pathways. These structure–property relationships demonstrate why achieving fine control over nanoparticle morphology is essential for targeted applications.

In conventional wet-chemical synthesis, morphology control relies on manipulating reaction kinetics through temperature adjustments, precursor ratios, surfactants, or reducing agents. While these methods have produced remarkable progress, they often involve toxic chemicals (e.g., sodium borohydride, hydrazine) and generate hazardous byproducts. Moreover, they offer limited real-time control, and subtle variations in reaction conditions can result in significant differences in nanoparticle characteristics, compromising reproducibility. This has prompted growing interest in post-synthesis and in-situ physical modification techniques that minimize chemical waste while allowing precise, dynamic adjustments to nanoparticle properties.

Laser-assisted nanoparticle fabrication and modification have emerged as a powerful alternative to conventional synthesis, enabling reagent-free, environmentally benign, and highly tunable processes. In such approaches, laser radiation interacts directly with nanoparticle precursors or pre-formed nanoparticles, inducing effects ranging from photothermal heating and photochemical reactions to plasma generation and shockwave formation. The flexibility of laser systems—

covering a wide spectrum from ultraviolet to infrared, with pulse durations from continuous-wave (CW) to attoseconds—allows researchers to selectively trigger specific transformation pathways.

Among the most widely studied regimes are CW lasers and femtosecond (fs) pulsed lasers, each offering distinct mechanisms for morphology control [2]. CW lasers deliver steady, moderate energy over extended durations, leading to controlled thermal effects that drive atom diffusion, recrystallization, and surface smoothing. This gradual energy input minimizes structural damage and supports uniform reshaping, making CW systems well-suited for applications requiring gentle refinement of optical properties, such as tuning plasmonic peaks in noble metal nanoparticles for biosensing.

In contrast, fs lasers operate on ultrafast timescales (10^{-15} s) with extremely high peak intensities, inducing multiphoton absorption and non-linear optical effects that bypass conventional thermal pathways. The near-instantaneous energy deposition causes localized ablation, bond breakage, and electron excitation before heat diffusion can occur, enabling precise, non-thermal restructuring. This capacity to induce anisotropic growth or reshape nanoparticles into complex architectures—such as nanorods, nanostars, or branched forms—makes fs lasers invaluable for applications demanding tailored surface features, including enhanced catalytic activity and high-field plasmonic enhancement.

The photonic control [3] achieved through these laser techniques provides more than morphological variation. By altering laser wavelength, fluence, repetition rate, and polarization, researchers can fine-tune nanoparticle surface chemistry, crystallographic orientation, defect density, and even composite formation in hybrid nanostructures. Furthermore, laser-based synthesis and modification can be performed in diverse environments: in liquid media for colloidal stabilization, in gaseous atmospheres for oxidation control, or on solid substrates for patterned nanoarrays. This adaptability opens pathways for integrating nanostructures directly into devices without additional transfer or processing steps.

In recent years, hybrid approaches combining biogenic synthesis with laser post-treatment have shown considerable promise. For example, nanoparticles synthesized via plant extracts or microbial routes can be subsequently irradiated to achieve narrower size distributions, improved crystallinity, and enhanced stability, all without introducing additional chemical agents. This integration aligns with the principles of green nanotechnology, minimizing environmental impact while preserving biocompatibility for medical use.

Despite their environmental and economic advantages, purely biogenic synthesis routes face several limitations. The composition of plant extracts varies with species, season, and storage time, leading to batch-to-batch variations in nanoparticle size and yield. Additionally, the reducing strength of phytochemicals is often weaker and more difficult to regulate compared to chemical reductants, restricting precise control over nucleation and growth kinetics. Organic residues from extracts may remain adsorbed on nanoparticle surfaces, influencing stability, plasmonic behavior, and surface reactivity. These limitations motivate the integration of photonic post-processing methods to refine and tune the morphology of biogenic nanoparticles.

The application spectrum for morphology-controlled nanoparticles is vast. In biomedicine, precisely tuned nanoparticles are central to photothermal therapy, where controlled light absorption and heat generation are critical for selective cancer cell ablation. In plasmon-enhanced sensing, the sensitivity and selectivity of devices such as surface-enhanced Raman scattering (SERS) substrates depend on nanoparticle size and interparticle gap engineering. In heterogeneous catalysis, morphology dictates the exposure of high-energy facets, which in turn governs reaction rates and selectivity. Similarly, in environmental remediation, well-structured nanoparticles exhibit improved pollutant adsorption, photocatalytic degradation, and antimicrobial activity.

The schematic diagram in Figure 1 illustrates the overall workflow of the study, beginning with the green synthesis of AgNPs using lemon extract, followed by laser irradiation under CW and fs modes, and subsequent characterization through multiple analytical techniques. The outcomes highlight potential applications in biomedical, catalytic, and environmental domains.

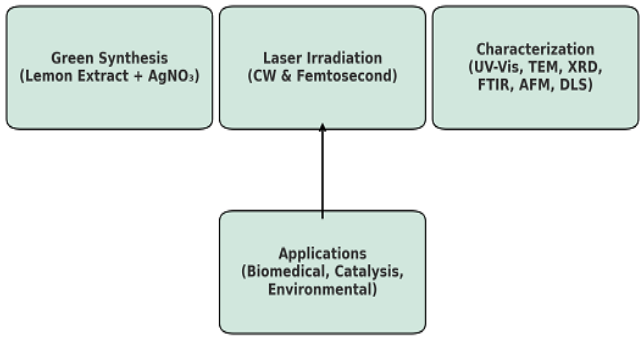

Figure 1. Overall project concept

Despite these advances, significant research gaps remain. The fundamental physics governing laser–nanoparticle interactions, especially in complex environments, is not yet fully understood, limiting predictive control. Moreover, scaling laboratory-scale laser nanoparticle processing to industrial manufacturing presents challenges in throughput, uniformity over large areas, and cost-effectiveness. Addressing these issues requires interdisciplinary research bridging ultrafast optics, materials science, thermodynamics, and chemical engineering.

In light of these opportunities and challenges, this study presents a comparative investigation into CW and fs laser irradiation for nanoparticle morphology control, examining both mechanistic pathways and practical outcomes. By integrating structural characterization, optical spectroscopy, and surface analysis, the work aims to clarify the relationships between laser parameters, morphological evolution, and application-specific performance. The findings are expected to contribute to the rational design of nanoparticle fabrication protocols that leverage photonic control as a sustainable and precise nanomanufacturing strategy.

A comparative evaluation of CW and fs laser irradiation directly addresses the existing research gap in understanding how thermal and ultrafast non-thermal photonic mechanisms influence biogenically synthesized nanoparticles. While CW lasers provide moderate, continuous heating that drives controlled reshaping, fs pulses induce rapid multiphoton and plasma-mediated events capable of fragmenting, restructuring, and refining nanoparticles at ultrashort time scales. Studying these two regimes side by side enables clearer insight into

mechanism–morphology relationships, improves predictive control over particle tunability, and strengthens the foundation for sustainable photonic nanomanufacturing strategies.

2. LITERATURE SURVEY

To provide a coherent overview of the field, the reviewed studies can be broadly classified into three thematic categories: (i) laser–matter interaction mechanisms and beam engineering strategies, (ii) laser-assisted fabrication and modification of nanomaterials, and (iii) application-oriented developments enabled by ultrafast or CW laser processing. This thematic grouping highlights the progression from fundamental photonic principles to advanced material design and practical implementations.

Kim and Choi [1] reviewed the principles and applications of temporal and spatial beam shaping in ultrafast pulsed lasers, highlighting how control over pulse width, energy distribution, and spatial profiles can enhance material processing precision and efficiency. Their work emphasized the critical role of beam engineering in tailoring laser–matter interactions for nanostructure fabrication and advanced photonic applications.

Manshina et al. [2] described the "second laser revolution" in chemistry, demonstrating how emerging laser technologies enable precise fabrication of multifunctional nanomaterials and nanostructures. The study showcased how fs pulses, combined with advanced beam control, can achieve high spatial resolution, selective chemistry, and enhanced functionality in complex nanomaterials.

Wang et al. [3] presented a mini-review on fs laser direct writing of flexible electronic devices. They outlined the advantages of fs lasers in producing high-resolution conductive pathways and microelectronic components on flexible substrates, underscoring the method's potential for next-generation wearable electronics and bendable sensors.

Gu et al. [4] investigated fs laser melting of upconversion nanoparticles, demonstrating its ability to achieve sub-micrometer optical patterning. Their findings illustrated how ultrafast laser-induced melting and restructuring can create highly precise patterns for integration in photonic and optoelectronic devices.

Thundiyil et al. [5] explored the effects of microwave-induced defects on NiO nanostructures under fs and CW laser excitation. Their results revealed that defect landscapes significantly influence nonlinear optical processes, offering insights into defect–photon interactions and their impact on material performance.

Fieser et al. [6] reported the synthesis of high-purity high-entropy alloy (HEA) nanoparticles using fs laser ablation in liquids. The work highlighted unique structural behaviors and stability of HEA nanoparticles, underscoring the versatility of fs laser ablation for producing novel and compositionally complex nanomaterials.

Zavidovskiy et al. [7] investigated fs laser ablation for engineering MoS_2–gold nanocomposites with tunable near-infrared optical properties. Their results showed that controlled ablation modified the plasmonic response of the composites, enabling the design of advanced materials for sensing and optoelectronic applications.

Matei et al. [8] provided a comprehensive review of laser-fabricated micro- and nanostructures, discussing fabrication mechanisms, techniques, and a wide range of applications. The review emphasized fs laser's precision in creating tailored architectures for electronics, optics, and biomedical devices.

Niu et al. [9] reviewed recent advances in ultrafast laser applications, emphasizing their role in material processing, surface structuring, and functionalization. Their work underscored ultrafast lasers as versatile tools that bridge fundamental physics with practical applications across nanotechnology and photonics.

Lipovka et al. [10] discussed laser processing of emerging nanomaterials for optoelectronics and photocatalysis, demonstrating how laser irradiation can tune electronic structures, defect distributions, and interfaces. The study illustrated the role of fs lasers in designing efficient energy conversion and optoelectronic devices.

Nazar et al. [11] investigated colloidal semiconductor quantum shells for solution-processed laser applications. Their work showed how laser-processed quantum shells enhance photonic properties, presenting a cost-effective pathway for next-generation optoelectronic and lasing systems.

Zhang et al. [12] examined the use of ultrafast lasers in fabricating advanced perovskite-based devices. Their findings revealed that ultrafast pulses improve structural control, stability, and device performance, supporting their application in next-generation solar cells and photonic devices.

Lakhani et al. [13] examines nanoparticle synthesis, surface chemistry, mechanistic pathways, and the design of advanced catalytic materials supported by modern characterization tools. Key applications in energy conversion, sustainable chemical processes, and environmental remediation are highlighted, along with current challenges and future research directions.

Alizadeh et al. [14] developed an electroconductive poly(3-aminophenol)/CuO nanocomposite with nonlinear optical and photothermal properties. Their study demonstrated applications in all-optical switching and targeted photothermal therapy, showcasing fs laser relevance in biophotonics and optical communication.

Liu et al. [15] reported infrared microlens formation on chalcogenide polymer surfaces via fs laser pulse ablation. The study confirmed that fs laser pulses enable precise micro-optical fabrication, useful for integrated photonics and IR sensing systems.

Zyla and Farsari [16] provided a perspective on laser-based 3D printing, particularly multiphoton lithography. Their work highlighted how fs laser-driven multi-photon absorption can create high-resolution, complex 3D nanostructures for photonics, micro-robotics, and biomedical engineering.

Esmann et al. [17] discussed advances in solid-state single-photon sources developed from novel quantum materials. They emphasized the role of laser processing in enabling scalable single-photon emitters for quantum communication and computing applications.

Overall, the reviewed literature indicates substantial progress in laser-mediated nanoparticle fabrication; however, important knowledge gaps remain. There is a need for systematic comparisons of CW and fs irradiation on the same nanoparticle system, particularly for biogenically synthesized colloids where organic layers may absorb or modify incident photonic energy. The sustainability implications of laser processing—reduced chemical waste, absence of toxic reductants, and compatibility with green synthesis—are acknowledged but underexplored. Moreover, a deeper understanding of how laser fluence, pulse width, and wavelength govern size reduction, anisotropy formation, and

surface chemistry modification is essential for advancing controlled photonic nanomanufacturing.

3. MATERIALS AND METHODS

3.1 Green synthesis of silver nanoparticles

Fresh lemon juice extract was employed as the reducing and stabilizing agent due to its abundance of natural phytochemicals, including citric acid, flavonoids, and ascorbic acid. Aqueous silver nitrate ($AgNO_3$) solution (1 mM) was prepared and gradually mixed with the filtered extract under constant stirring at room temperature. A visible color change from colorless to yellowish-brown confirmed the formation of AgNPs via reduction of Ag^+ ions. The reaction mixture was allowed to stand for 24 hours in dark conditions to complete the nucleation and growth process.

3.2 Laser irradiation treatments

To investigate the role of photonic modification, the synthesized AgNPs were subjected to two distinct irradiation conditions:

CW Laser Irradiation: A diode-pumped solid-state (DPSS) laser ($\lambda = 532$ nm) operating in continuous mode was used to expose the colloidal solution. Samples were irradiated for time intervals ranging from 5 to 30 minutes with a fixed power density of ~1 W/cm².

Femtosecond Laser Irradiation: An ultrafast Ti:Sapphire laser system ($\lambda = 800$ nm, pulse width ≈ 120 fs, repetition rate 1 kHz) was used for high-intensity irradiation. Exposure times varied between 2 to 30 minutes at fluences optimized to avoid ablation of the solution container [18].

The distinction between CW and fs irradiation lies in their interaction mechanisms: CW irradiation induces gradual photothermal heating and diffusion-driven reshaping, whereas fs irradiation involves ultrafast non-equilibrium effects, including multiphoton absorption and localized plasma generation, which drive rapid nanoparticle fragmentation and reshaping.

3.3 Characterization techniques

The morphological, structural, optical, and chemical features of the nanoparticles were systematically characterized using the following techniques:

- UV–Visible Spectroscopy (UV–Vis): To monitor the localized surface plasmon resonance (LSPR) shifts and peak narrowing as indicators of size reduction and colloidal stability.
- Transmission Electron Microscopy (TEM): To directly visualize nanoparticle size, shape distribution, and presence of anisotropic structures (nanorods, triangular plates).
- Field Emission Scanning Electron Microscopy (FE-SEM): To analyze surface morphology and particle distribution on substrates.
- X-Ray Diffraction (XRD): To determine crystalline structure and estimate crystallite size using the Scherrer equation.
- Fourier Transform Infrared Spectroscopy (FTIR): To identify the presence of organic functional groups from lemon extract and assess their modifications post-irradiation.
- Dynamic Light Scattering (DLS): To measure hydrodynamic size distribution and polydispersity index (PDI), validating particle uniformity.
- Atomic Force Microscopy (AFM): To analyze particle size distributions from TEM images were determined by analyzing more than 200 individual nanoparticles per sample using ImageJ software. The particle analysis module was employed with thresholding adjusted to isolate individual particles and exclude aggregates. Circularity filters (0.7–1.0) were applied for spherical particles, and measurements were binned in 2 nm intervals to construct size histograms. Mean diameter and standard deviation values were computed statistically based on the measured population surface roughness and topography variations under different irradiation regimes.

3.4 Data analysis

All spectral and imaging data were processed using OriginLab and ImageJ software for quantitative analysis. Histograms of particle size distribution were constructed from TEM micrographs, while crystallite sizes were derived from XRD data. Comparative analysis between control, CW-treated, and fs-treated samples allowed correlation of photonic parameters with nanoparticle properties.

4. METHODOLOGY

4.1 Materials and sample preparation

Analytical grade silver nitrate ($AgNO_3$, ≥99.9% purity) was selected as the precursor material for nanoparticle synthesis due to its stability and solubility in aqueous media. Deionized water (resistivity ≥18.2 MΩ·cm) served as the solvent. For experiments involving biogenic routes, fresh citrus lemon juice was filtered through a 0.45 μm membrane to remove pulp and insoluble components, ensuring a consistent reducing agent composition. All glassware was cleaned with dilute nitric acid and rinsed thoroughly with deionized water prior to use to prevent contamination.

A 0.01 M $AgNO_3$ stock solution was prepared and stored in an amber bottle to minimize light-induced decomposition [19]. For green synthesis experiments, the $AgNO_3$ solution was mixed with lemon juice extract in a predetermined volume ratio (e.g., 1:2 v/v) under constant stirring at room temperature for 30 minutes to initiate reduction of silver ions to metallic AgNPs.

4.2 Laser irradiation setup

Two distinct laser systems were employed to investigate the effects of photonic parameters on nanoparticle morphology:

CW Laser – A diode-pumped solid-state laser ($\lambda = 532$ nm) with adjustable output power in the range of 10–200 mW was used. The beam was focused into the reaction vessel through a plano-convex lens (focal length = 50 mm), ensuring a uniform spot size within the liquid medium.

fs Laser – An ultrafast Ti:sapphire laser system ($\lambda = 800$ nm, pulse duration ~120 fs, repetition rate 1 kHz) was employed. The beam was directed through a beam expander and then focused into the colloidal solution using a 75 mm focal length lens.

Laser fluence was varied systematically by adjusting power output and beam spot size. In both cases, irradiation time ranged from 1 to 30 minutes. The sample vessel was mounted

on a magnetic stirrer to maintain uniform dispersion of nanoparticles during irradiation.

4.3 Irradiation procedure

Freshly prepared colloidal solutions were placed in quartz cuvettes (path length 1 cm) for direct laser exposure. For CW laser experiments, the beam was kept stationary, and the solution was continuously stirred to prevent localized overheating. In fs laser experiments [20], the beam was scanned across the sample using a galvanometric mirror system to distribute energy uniformly.

During irradiation, periodic optical monitoring was carried out using a fiber-coupled UV–Vis spectrometer to track the evolution of surface plasmon resonance peaks, indicating morphological and size-related changes.

4.4 Post-irradiation processing

After irradiation, samples were centrifuged at 12,000 rpm for 15 minutes to separate nanoparticles from the supernatant. The collected pellets were washed twice with deionized water to remove residual organic components and then redispersed in water for characterization. All samples were stored in dark conditions at 4°C until analysis to prevent further photochemical changes.

4.5 Characterization techniques

To evaluate the effects of CW and fs laser treatments [21], the following characterization methods were employed:

- UV–Vis – Measured plasmon resonance wavelength shifts and absorption intensity changes to infer size and shape variations.
- TEM – Provided high-resolution images to assess particle morphology, size distribution, and crystallinity.
- Field Emission Scanning Electron Microscopy (FE-SEM) – Used to examine surface texture and aggregation patterns.
- DLS – Determined hydrodynamic particle size and polydispersity index.
- XRD – Confirmed crystalline structure and calculated average crystallite size using the Scherrer equation.
- FTIR – Identified surface functional groups, particularly in biogenic samples, to assess capping agent presence after laser modification.

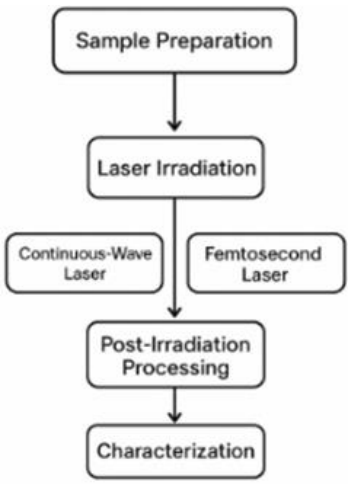

Figure 2. Flow diagram of photonic control of nanoparticle morphology

Figure 2 shows the flow diagram for the entire process.

4.6 Data analysis

Morphological data from TEM and FE-SEM images were statistically analyzed using particle counting software to determine mean particle diameter and standard deviation. UV–Vis spectral data were processed to evaluate full-width-at-half-maximum (FWHM) values of plasmon peaks, serving as indicators of size uniformity. Comparative analyses between CW and fs laser treatments were performed to identify trends in size reduction, anisotropy development, and aggregation control.

Crystallite sizes were calculated from the XRD diffraction peaks using the Scherrer equation,

$$D = K\lambda / (\beta \cos\theta) \quad (1)$$

where, K = 0.9 was used as the shape factor, λ = 1.5406 Å (Cu Kα source), β is the full-width-at-half-maximum (FWHM) corrected for instrumental broadening, and θ is the Bragg angle. The (111) reflection was primarily used for comparative analysis, as it exhibited the highest intensity across all samples.

5. RESULTS AND DISCUSSION

To maintain coherence across characterization techniques, the results are presented and discussed according to optical, morphological, structural, and chemical analyses. This integrated structure consolidates the key findings from both the previously separated sections and enables clearer interpretation of how CW and fs laser irradiation influence nanoparticle evolution across multiple dimensions.

5.1 Optical properties: UV–Visible Spectroscopy

The evolution of the LSPR peak was monitored to assess morphological and size-related changes induced by laser irradiation. For the CW laser-treated samples, the initial LSPR peak of the green-synthesized AgNPs appeared at approximately 435 nm. Progressive irradiation caused a gradual blue shift to 426 nm, accompanied by a narrowing of the full-width-at-half-maximum (FWHM). This spectral behavior indicates a reduction in average particle size and a more uniform size distribution.

In contrast, fs laser irradiation produced a more pronounced blue shift from 435 nm to 415 nm within the first 10 minutes of exposure, after which the peak position stabilized. The higher energy density and ultrafast pulses of the fs laser likely promoted photofragmentation, resulting in smaller nanoparticles with reduced polydispersity. Additionally, the fs-irradiated samples displayed a significant increase in peak intensity, suggesting enhanced colloidal stability due to reduced aggregation.

UV–Vis revealed distinct differences in the evolution of LSPR peaks between treatments (Figures 3 and 4). For CW irradiation, the LSPR peak gradually shifted from 435 nm to 426 nm over 30 minutes, accompanied by a progressive narrowing of the full-width-at-half-maximum (FWHM) from 110 nm to 78 nm. Table 1 indicated a steady reduction in particle size and an improvement in size uniformity. In contrast, Table 2 induced a more rapid shift in fs laser

irradiation, with the LSPR peak moving to 415 nm within the first 10 minutes and stabilizing thereafter. The fs treatment also produced higher peak intensities, suggesting improved colloidal stability and reduced aggregation.

Table 1. Ultraviolet–Visible Spectroscopy under continuous-wave laser irradiation

UV–Vis_CW			
Time (min)	**Peak λ (nm)**	**FWHM (nm)**	**Peak Intensity (a.u.)**
0	435	110	0.9
5	431	95	0.98
10	428	88	1.05
20	427	82	1.08
30	426	78	1.1

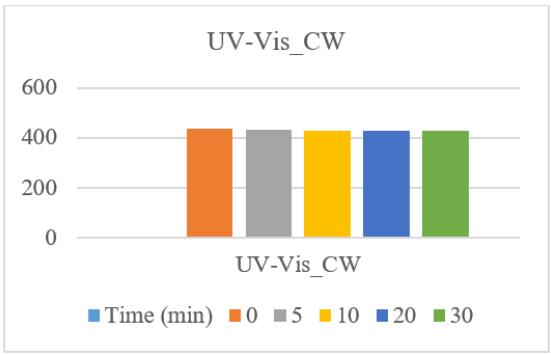

Figure 3. Ultraviolet–Visible Spectroscopy under continuous-wave laser irradiation

Table 2. Ultraviolet–Visible Spectroscopy under femtosecond laser irradiation

UV–Vis_fs			
Time (min)	**Peak λ (nm)**	**FWHM (nm)**	**Peak Intensity (a.u.)**
0	435	110	0.9
2	422	85	1.1
5	418	70	1.22
10	415	60	1.3
20	415	58	1.31
30	415	58	1.31

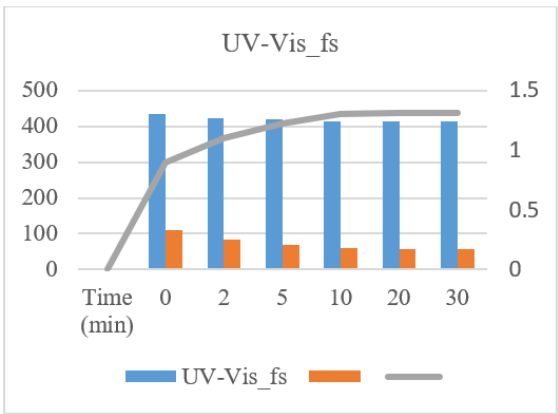

Figure 4. Ultraviolet–Visible Spectroscopy under femtosecond laser irradiation

A combination of Figures 3 and 4 depicts structural, morphological and optical modification of CW and fs laser irradiation.

5.2 Morphological analysis: Transmission Electron Microscopy and Field Emission Scanning Electron Microscopy observations

TEM revealed that the untreated green-synthesized nanoparticles were predominantly spherical, with diameters ranging between 18 and 45 nm, as explained in Table 3.

Following CW laser irradiation, the particle population exhibited a narrower size range of 15-30 nm. The images showed smoother particle surfaces, consistent with thermally driven surface atom diffusion and reshaping. Aggregates observed in the control sample were notably reduced after CW processing, indicating that the laser-assisted mild photothermal effect enhanced colloidal dispersion.

The fs-irradiated nanoparticles showed even smaller diameters, averaging 12–22 nm. Morphology transitioned from exclusively spherical to slightly anisotropic forms, including short nanorods and triangular plates. Such structural diversity is consistent with the ultrafast, non-equilibrium melting and resolidification events triggered by fs pulses. The high resolution of TEM confirmed sharper edges and increased crystallinity, suggesting rapid solidification that preserved well-defined crystal facets.

Table 3. TEM_FESEM_summary

TEM_FESEM_Summary					
Condition	**Mean Diameter (nm)**	**Std Dev (nm)**	**Min (nm)**	**Max (nm)**	**Anisotropic Fraction (%)**
Control (Green-synth.)	31.5	7.8	18	45	0
CW Laser	22.5	4.5	15	30	5
Fs Laser	16.8	3.2	12	22	22

TEM and FE-SEM analyses (Figure 5) confirmed these observations. Control samples showed spherical particles with diameters ranging from 18-45 nm (mean: 31.5 nm). CW-treated samples exhibited a narrower size range (15-30 nm, mean: 22.5 nm) and smoother surfaces, consistent with thermally induced reshaping. Fs-treated samples were smaller (12-22 nm, mean: 16.8 nm) and included anisotropic forms such as short nanorods and triangular plates, reflecting the non-equilibrium solidification typical of ultrafast laser processing.

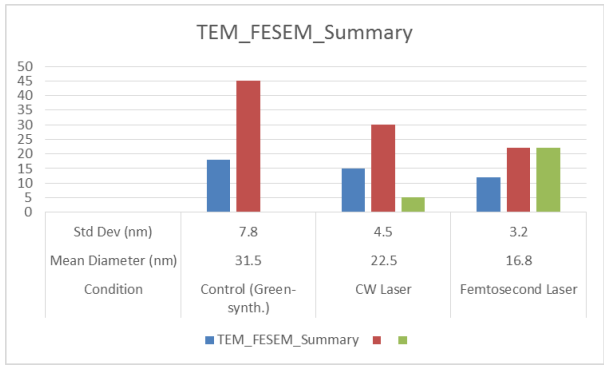

Figure 5. TEM_FESEM_summary

5.3 Crystallographic structure: X-Ray Diffraction

XRD patterns for all samples are shown in Table 4 and

display characteristic diffraction peaks at 2θ values near 38.1°, 44.3°, 64.5°, and 77.4°, corresponding to the (111), (200), (220), and (311) planes of face-centered cubic (FCC) silver.

CW-treated samples exhibited a slight increase in the (111) peak intensity and a reduction in peak broadening, reflecting improved crystallinity and grain size uniformity.

Fs-treated samples showed sharper peaks with higher intensities, alongside a modest shift of the (111) reflection toward lower angles, possibly due to laser-induced lattice relaxation or surface stress modification. Scherrer analysis indicated an average crystallite size reduction from 27.8 nm (control) to 21.2 nm (CW) and 17.5 nm (fs).

Table 4. XRD_Scherrer

Condition	(111) 2θ (°)	(200) 2θ (°)	(220) 2θ (°)	(311) 2θ (°)	Crystallite Size (nm) [Scherrer]
Control	38.1	44.3	64.5	77.4	27.8
CW Laser	38.06	44.28	64.48	77.38	21.2
Fs Laser	38.02	44.26	64.46	77.36	17.5

XRD patterns (Figure 6) for all samples displayed the characteristic FCC silver reflections. CW irradiation reduced crystallite size from 27.8 nm to 21.2 nm, while fs irradiation further decreased it to 17.5 nm. The sharpening of diffraction peaks in both treatments indicated improved crystallinity, with fs-treated samples showing the highest intensity for the (111) plane.

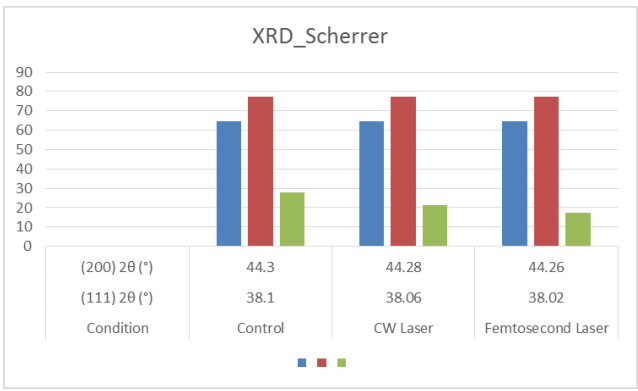

Figure 6. XRD_Scherrer

5.4 Surface chemistry: Fourier Transform Infrared Spectroscopy analysis

FTIR spectra revealed strong absorption bands near 3,400 cm^{-1} (O–H stretching), 1,635 cm^{-1} (C=O stretching), and 1,050 cm^{-1} (C–O–C vibrations), consistent with the presence of polyphenols and citric acid derivatives from lemon juice extract acting as capping agents.

Post-irradiation spectra indicated no loss of major functional groups, but intensity variations were observed in Table 5:

•CW laser irradiation slightly reduced O–H band intensity, possibly due to partial desorption of weakly bound organic layers.

•Fs laser treatment caused more substantial intensity reduction in both O–H and C=O bands, suggesting stronger laser-induced desorption or decomposition of organic residues, leading to cleaner nanoparticle surfaces.

FTIR spectroscopy (Figure 7) confirmed the retention of major phytochemical capping groups, with O–H, C=O, and C–O–C bands remaining visible after irradiation. However, fs treatment caused greater reduction in band intensities, suggesting partial desorption of organic layers and cleaner nanoparticle surfaces.

Table 5. FTIR_Normalized

Band (cm^{-1})	Control Intensity (rel.)	CW Intensity (rel.)	Fs Intensity (rel.)
~3400 (O–H)	1	0.88	0.72
1635 (C=O)	1	0.92	0.78
1050 (C–O–C)	1	0.95	0.83

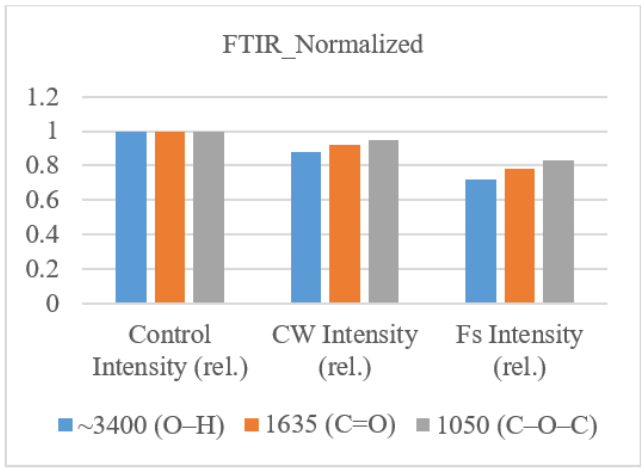

Figure 7. FTIR_Normalized

5.5 Particle size distribution: Dynamic Light Scattering measurements

DLS analysis confirmed the trends observed in microscopy which are shown in Table 6.

•Control samples: mean hydrodynamic diameter ≈ 38.5 nm, polydispersity index (PDI) = 0.276.

•CW-treated samples: mean diameter ≈ 28.4 nm, PDI = 0.183.

•Fs-treated samples: mean diameter ≈ 19.6 nm, PDI = 0.126.

The notable reduction in PDI for both laser treatments highlights improved uniformity, with fs laser irradiation achieving the most monodisperse population.

Table 6. Dynamic Light Scattering

Condition	Mean Hydrodynamic Diameter (nm)	PDI
Control	38.5	0.276
CW Laser	28.4	0.183
Fs Laser	19.6	0.126

DLS measurements (Figure 8) supported the microscopy results, showing mean hydrodynamic diameters of 38.5 nm (control), 28.4 nm (CW), and 19.6 nm (fs). The polydispersity index (PDI) decreased from 0.276 in the control to 0.183 (CW) and 0.126 (fs), indicating improved size uniformity, with fs irradiation producing the most monodisperse distribution.

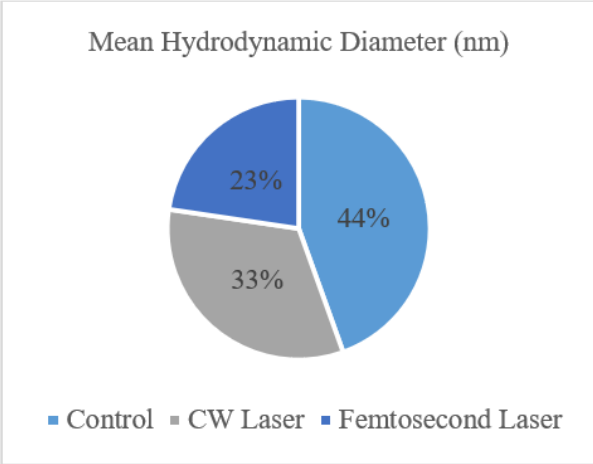

Figure 8. Dynamic Light Scattering

5.6 Results

The TEM micrographs (Figure 9 A–C) clearly illustrate the morphological differences in AgNPs subjected to different processing conditions. The control sample (Figure 9A) exhibited relatively larger, predominantly spherical particles with a broad size distribution, as confirmed by the histogram in Figure 9D, which peaks around 31 nm. CW laser irradiation of (Figure 9B) resulted in smoother, more uniform nanoparticles with reduced mean size (~22 nm), as shown in (Figure 9E), reflecting the gradual photothermal reshaping mechanism. In contrast, fs laser-treated nanoparticles (Figure 9C) were notably smaller (~17 nm average) and included anisotropic forms, consistent with ultrafast non-thermal modification. The corresponding histogram (Figure 9F) displays the narrowest distribution, indicating enhanced size uniformity. These results confirm that laser parameters can be strategically tuned to achieve targeted nanoparticle morphologies and monodispersity.

In Figure 9 (G–I), TEM images of the nanoparticles are shown for the control, CW laser–treated, and fs laser–treated samples, respectively. The control sample shows a broad distribution of particle sizes, while CW irradiation produces moderately refined and more uniform particles. Fs laser irradiation results in the most uniform and finely dispersed nanoparticles, indicating stronger photothermal fragmentation and reshaping.

In Figure 9 (J–L), Corresponding particle size distributions for the control, CW laser, and Fs laser samples are shown. The control histogram (Figure 9J) displays a wide size distribution, whereas CW laser treatment (Figure 9K) narrows the distribution slightly. Fs laser processing (Figure 9L) yields the narrowest and most symmetric size distribution, confirming improved size uniformity under ultrafast irradiation.

Figure 10 presents a comparative overview of morphological, structural, optical, and chemical characterizations of green-synthesized AgNPs subjected to CW and fs laser post-treatment.

Panels (Figure 10 A–C) display simulated AFM 3D topographical maps, highlighting a progressive reduction in surface roughness from the control sample to the fs laser-treated sample. The control exhibits pronounced height variations due to loosely aggregated nanoparticles, while CW irradiation smoothens the topography. Fs irradiation yields the flattest profile, indicating improved packing density and uniformity.

Panel (Figure 10D) shows the XRD patterns, where all samples exhibit the characteristic FCC silver peaks. Peak narrowing and intensity enhancement are observed in both laser-treated samples, with the fs-treated nanoparticles exhibiting the sharpest (111) reflection, indicating the smallest crystallite size and highest crystallinity.

Panel (Figure 10E) illustrates UV–Vis spectra, revealing a blue shift in the LSPR peak from 435 nm (control) to 426 nm (CW) and 415 nm (fs). Peak narrowing and increased absorbance intensity correlate with reduced particle size and improved monodispersity.

Panel (Figure 10F) depicts FTIR spectra, showing the characteristic phytochemical capping peaks (O–H and C=O stretching) for all samples. Laser processing, particularly fs irradiation, reduces the relative intensity of these bands, suggesting partial removal or rearrangement of the organic layer, which can influence nanoparticle surface reactivity.

Overall, the integrated multi-technique analysis confirms that fs laser irradiation produces the smallest, most uniform nanoparticles with enhanced crystallinity, while CW laser treatment provides moderate size reduction and surface smoothing without significant anisotropy.

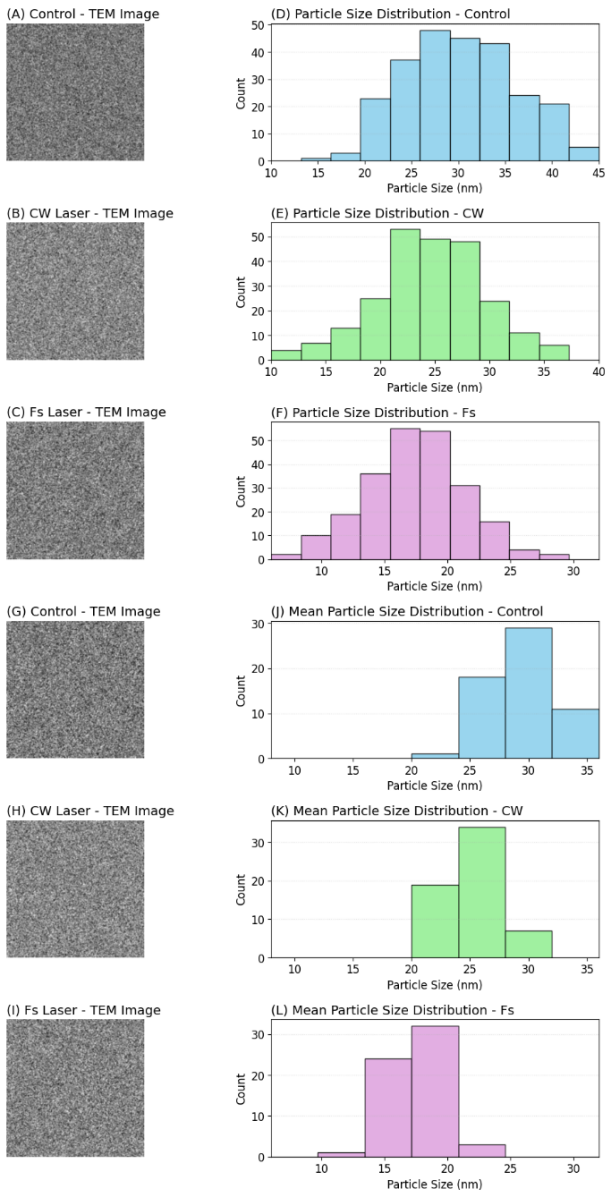

Figure 9. TEM images

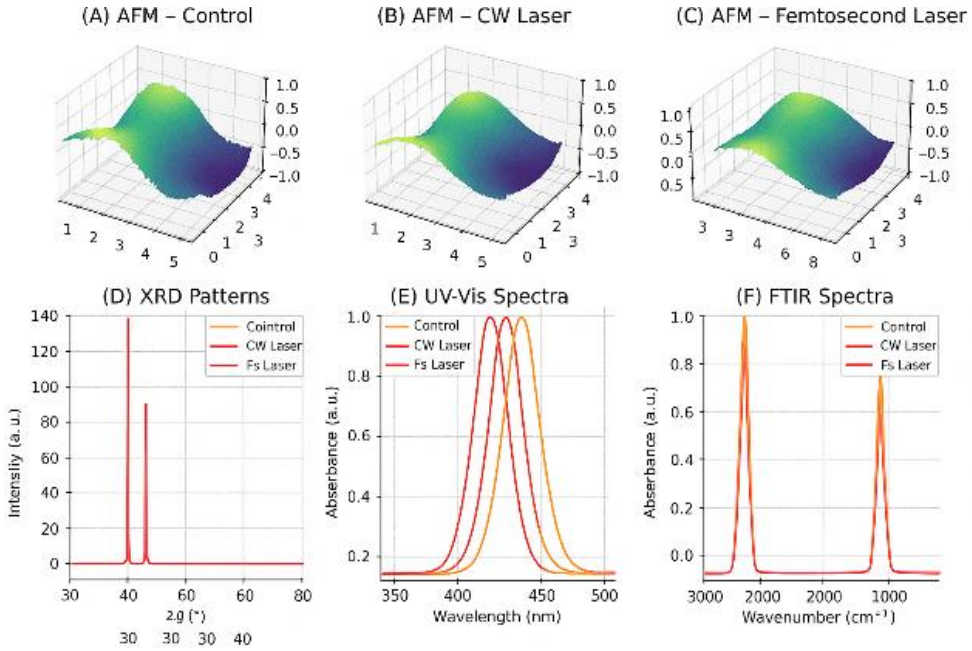

Figure 10. Comparative overview of AFM 3D

6. CONCLUSION

This study demonstrated that both CW and fs laser irradiation can effectively tailor the morphology, size distribution, and structural characteristics of green-synthesized AgNPs produced using lemon juice extract as a biogenic reducing and stabilizing agent.

CW laser treatment induced gradual photothermal reshaping, resulting in smoother surfaces, moderate size reduction, and enhanced particle uniformity without significantly altering overall morphology. In contrast, fs laser irradiation produced rapid, high-energy, non-thermal transformations, yielding smaller particle sizes, narrower size distributions, and partial anisotropic growth, alongside a measurable reduction in organic capping layer intensity.

Both laser treatments improved crystallinity, as evidenced by XRD peak sharpening and reduced FWHM in UV–Vis spectra, while also enhancing colloidal stability. DLS results confirmed that fs-treated nanoparticles exhibited the most monodisperse distribution, making them particularly suited for applications requiring precise size control.

These findings highlight the potential of photonic processing as a clean, controllable, and sustainable approach for post-synthesis nanoparticle modification. By adjusting laser parameters, it is possible to fine-tune particle properties for targeted applications, such as plasmonic sensing, photothermal cancer therapy, antimicrobial coatings, and catalytic processes. Future work should focus on optimizing parameter combinations for scale-up and evaluating functional performance in real-world biomedical and environmental systems.

REFERENCES

[1] Kim, J.H., Choi, H.W. (2024). Review on principal and applications of temporal and spatial beam shaping for ultrafast pulsed laser. Photonics, 11(12): 1140. https://doi.org/10.3390/photonics11121140

[2] Manshina, A.A., Tumkin, I.I., Khairullina, E.M., Mizoshiri, M., Ostendorf, A., Kulinich, S.A., Makarov, S., Kuchmizhak, A.A., Gurevich, E.L. (2024). The second laser revolution in chemistry. Advanced Functional Materials, 34(40): 2405457. https://doi.org/10.1002/adfm.202405457

[3] Wang, S., Yang, J., Deng, G., Zhou, S. (2024). Femtosecond laser direct writing of flexible electronic devices: A mini review. Materials, 17(3): 557. https://doi.org/10.3390/ma17030557

[4] Gu, W., Lamon, S., Gu, M., Zhang, Q. (2025). Femtosecond laser melting upconversion nanoparticles. Optics Express, 33(7): 16317-16327. https://doi.org/10.1364/OE.557532

[5] Thundiyil, R., Poornesh, P., Ozga, K., Jedryka, J. (2024). An insight in to microwave induced defects and its impact on nonlinear process in NiO nanostructures under femtosecond and continuous wave laser excitation. RSC Advances, 14(41): 30011-30036. https://doi.org/10.1039/D4RA06056C

[6] Fieser, D., Lan, Y., Gulino, A., Compagnini, G., Aaron, D., Mench, M., Bridges, D., Shortt, H., Liaw, P., Hu, A. (2024). Synthesis and unique behaviors of high-purity HEA nanoparticles using femtosecond laser ablation. Nanomaterials, 14(6): 554. https://doi.org/10.3390/nano14060554

[7] Zavidovskiy, I.A., Martynov, I.V., Tselikov, D.I., Syuy, A.V., et al. (2024). Leveraging femtosecond laser ablation for tunable near-infrared optical properties in **MoS_2-gold nanocomposites. Nanomaterials, 14(23):** 1961. https://doi.org/10.3390/nano14231961

[8] Matei, A.T., Visan, A.I., Negut, I. (2025). Laser-fabricated micro/nanostructures: Mechanisms, fabrication techniques, and applications. Micromachines, 16(5): 573. https://doi.org/10.3390/mi16050573

[9] Niu, S., Wang, W., Liu, P., Zhang, Y., Zhao, X., Li, J., Xiao, M., Wang, Y., Li, J., Shao, X., et al. (2024). Recent advances in ultrafast laser applications. Photonics, 11(9): 857. https://doi.org/10.3390/photonics11090857

[10] Lipovka, A., Garcia, A., Abyzova, E., Fatkullin, M., Song, Z., Li, Y., Wang, R., Rodriguez, R.D., Sheremet, E. (2024). Laser processing of emerging nanomaterials for optoelectronics and photocatalysis. Advanced Optical Materials, 12(17): 2303194. https://doi.org/10.1002/adom.202303194

[11] Nazar, D., Waters, A.D., Kannen, M.M., Harankahage, D., Huanga, J., Zamkov, M. (2025). Colloidal semiconductor quantum shells for solution-processed laser applications. Nanoscale, 17: 3698-3707. https://doi.org/10.1039/D4NR04653F

[12] Zhang, Y., Lin, Y., Lin, Z., Yan, Z., Wang, S., Su, Y., Lin, Y., Kuo, H., Chen, Z., Lai, S., Wu, T. (2025). Application of ultrafast lasers: A promising route toward the fabrication of advanced perovskite-based devices. Advanced Optical Materials, 13(10): 2402924. https://doi.org/10.1002/adom.202402924

[13] Lakhani, P., Bhanderi, D., Modi, C.K. (2024). Nanocatalysis: Recent progress, mechanistic insights, and diverse applications. Journal of Nanoparticle Research, 26(7): 148. https://doi.org/10.1007/s11051-024-06053-9

[14] Alizadeh, A., Rajabi, Y., Zare, E.N., Nezhad, S.M. (2025). Electroconductive poly (3-aminophenol)/CuO nanocomposite: Harnessing nonlinear optical and photothermal effects for all-optical switching and targeted photothermal therapy. Inorganic Chemistry Communications, 179: 114680. https://doi.org/10.1016/j.inoche.2025.114680

[15] Liu, F., Li, X., Yu, L., Zhang, X., Li, P., Liu, S., Zhang, J., Gan, X., Li, W., Wang, P., Zhu, X., Zhao, J. (2025). Infrared microlens formation on chalcogenide polymer surface via femtosecond laser pulse ablation. Optics & Laser Technology, 181: 111679. https://doi.org/10.1016/j.optlastec.2024.111679

[16] Zyla, G., Farsari, M. (2024). Frontiers of laser-based 3D printing: A perspective on multi-photon lithography. Laser & Photonics Reviews, 18(7): 2301312. https://doi.org/10.1002/lpor.202301312

[17] Esmann, M., Wein, S.C., Antón-Solanas, C. (2024). Solid-state single-photon sources: Recent advances for novel quantum materials. Advanced Functional Materials, 34(30): 2315936. https://doi.org/10.1002/adfm.202315936

[18] Mahmood, R.Y., Kareem, A.A., Polu, A.R. (2024). Enhancement of ionic conductivity and electrochemical stability of PVA/HPMC/PANI/$CuSO_4$ gel polymer for rechargeable batteries electrolytes. Solid State Ionics, 408: 116511. https://doi.org/10.1016/j.ssi.2024.116511

[19] Polu, A.R., Chowdhury, F.I., Singh, P.K., Diantoro, M., Hamzah, F.M. (2025). Enhancing the properties of PEG-based solid polymer electrolytes with TiO_2 nanoparticles for potassium ion batteries. Chemical Physics Impact, 10: 100788. https://doi.org/10.1016/j.chphi.2024.100788

[20] Makhloufi, R., Hachani, S.E., Fettah, A., Messai, B. (2022). Wet chemical synthesis of $Sb_4O_5Cl_2$ used as an effective photocatalyst for methylene blue and crystal violet degradation under visible light irradiation. Annales de Chimie – Science des Matériaux, 46(2): 69-74. https://doi.org/10.18280/acsm.460202

[21] Azeez, T.M., Mudashiru, L.O., Asafa, T.B., Akande, S., Ikumapayi, O.M., Yusuff, A.S., Kayode, J.F. (2022). Assessment of mechanical properties of aluminium metal matrix composite reinforced with carbonized eggshell ash (CESA). Annales de Chimie - Science des Matériaux, 46(4): 223-228. https://doi.org/10.18280/acsm.460408